Batteries & Supercaps

Research Article
doi.org/10.1002/batt.202300591

Chemistry Europe
European Chemical Societies Publishing

www.batteries-supercaps.org

Investigating the Role of a P(VDF–TrFE) Ferroelectric Separator in Li-Metal Pouch Cells using Electrochemical Impedance Spectroscopy

Leonardo Pires Da Veiga,*[a] Shubam Sharad Bhoir,[a] Dominic Brüllmann,[a] Samuel Malburet,[b] Simon Müller,[c] Micheal Stalder,[c] Claudio Brivio,[a] and Andrea Ingenito*[a]

This study explores the efficacy of employing P(VDF–TrFE), a ferroelectric copolymer, to mitigate the formation of dead lithium in Li-metal anodes when paired with carbonate electrolytes. Employing non-solvent induced phase separation (NIPS), self-standing membranes and coatings on polypropylene (PP) separators were prepared, both demonstrating a homogenous cellular pore structure and excellent ionic conductivity. Rigorous evaluation in pouch cell formats, featuring a thin Li-metal anode (50 μm), a high-loading NMC532 cathode (3 mAhcm^{-2}), and a carbonate electrolyte, reveals the superior performance of cells with P(VDF–TrFE)-coated PP separators. Notably, these cells exhibit slower and more consistent capacity fading, as well as the weakest increase in impedance, as evidenced by Electrochemical Impedance Spectroscopy (EIS) investigations. This work underscores the promising role of P(VDF–TrFE) as a key material for addressing challenges associated with dead lithium, offering valuable insights for advancing Li-metal battery technologies in practical applications.

Introduction

Following the rapid penetration of electric vehicles in the automotive market, a pressing need has been raised to increase the energy density of Li-ion batteries continuously to increase driving range.[1,2] Among the possible strategies, the replacement of the graphite anode with a Li-metal electrode is widely considered one of the most promising solutions.[3,4] Unlike graphite anodes that rely on intercalation chemistry, Li-metal batteries store energy through the plating of Li at the interface with the electrolyte.[5–7] This fundamental distinction lies at the core of the challenges facing Li-metal. The process of Li-plating induces a significant volumetric expansion of the anode, commonly referred to as 'breathing', leading to persistent cracks in the solid electrolyte interphase (SEI). This causes continuous exposure of freshly plated Li to the liquid electrolyte, which in turn is immediately reduced, forming a new SEI.[8] Moreover, planar and dense plating of metallic Li on a Li-metal anode has not been observed so far in carbonate electrolytes, as typically, Li tends to plate in the form of dendrites.[9,10] The sequential charging and discharging of the cell exacerbate the surface instability of Li-metal, giving rise to the formation of what is commonly called 'dead Li'.[11] The continuous formation of SEI and dead Li represent the primary contributors to the depletion of Li inventory. Both effects together lead to capacity fading, an increase of internal resistance, an increased risk of internal short circuits by dendrite penetration, electrolyte depletion, continuous gas generation, and an increase in cell thickness.[12] Effectively addressing mossy Li and Li dendrites stands as a pivotal factor in unlocking the full potential of Li-metal batteries, and enabling widespread adoption in the automotive market. Researchers are actively pursuing two main solutions: physical obstruction through the use of rigid electrolytes[13,14] or thermodynamic suppression strategies.[15,16]

Efforts to suppress lithium dendrites have introduced the innovative concept of leveraging ferroelectric materials.[17–22] Notably, a series of articles have explored the application of ferroelectric poly(vinylidene fluoride) (PVDF) as a separator membrane.[23,24] For commercially available olefine separators like polyethylene (PE) and polypropylene (PP), films are extruded and stretched at multiple temperatures to form a microporous structure.[24–26] In the case of PVDF-based membranes, alternative solvent-based procedures have been developed, such as nonsolvent-induced phase separation (NIPS),[27,28] shown in Figure 1. The NIPS technique utilizes three main components: the polymer, the solvent (in which the polymer is soluble), and the non-solvent (in which the polymer is insoluble,

[a] L. Pires Da Veiga, S. Sharad Bhoir, D. Brüllmann, C. Brivio, A. Ingenito
Sustainable Energy Center
Centre suisse d'électronique et de microtechnique
Rue de Monruz 17, 2000 Neuchâtel
E-mail: leonardo.piresdaveiga@csem.ch
andrea.ingentio@csem.ch

[b] S. Malburet
SPECIFIC POLYMERS
150 Avenue des Cocardières, 34160, Castries, France

[c] S. Müller, M. Stalder
Institute for Intelligent Industrial Systems
Bern University of Applied Sciences
Pestalozzistrasse 20, 3400 Burgdorf, Switzerland

Supporting information for this article is available on the WWW under https://doi.org/10.1002/batt.202300591

Research Article
doi.org/10.1002/batt.202300591
Chemistry Europe
European Chemical Societies Publishing

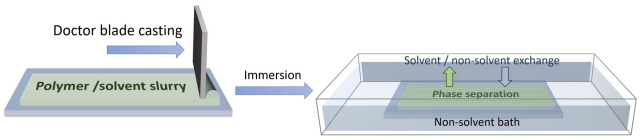

Figure 1. The production of a porous membrane by nonsolvent-induced phase separation (NIPS).

but the solvent is soluble).[29] The process begins with the dissolution of the polymer in the solvent, forming a homogeneous solution, which is then cast into a film on a substrate. Subsequently, the substrate is immersed in a coagulation bath containing the non-solvent. As the non-solvent replaces the solvent, phase separation ensues, resulting in a polymer-lean phase and a polymer-rich phase. Over time, the polymer-rich phase undergoes solidification through processes such as gelation, vitrification, and crystallization, ultimately forming the solid membrane matrix. The polymer-lean domains, once the film is extracted from the bath and dried, transform into the pores within the resulting membrane.

Herein we demonstrate a novel application of the NIPS method to fabricate a porous ferroelectric coating on a porous separator. We showcase the coated separator with respect to a conventional ferroelectric separator in single-layer Li-metal pouch cells. We selected a ferroelectric copolymer of PVDF, namely poly(vinylidene fluoride-co-trifluoroethylene) (P-(VDF–TrFE)). While PVDF crystallizes mostly in α-PVDF, P-(VDF–TrFE) is designed to take advantage of the steric hindrance of the TrFE group to penalize the α-PVDF phase, hence promoting the β-PVDF phase. The former is non-polar, while the latter is polar. This difference gives ferroelectric properties to the polymer.[30]

For the qualitative evaluation of the advantages offered by the separator, post-mortem digital imaging and SEM imaging is performed. Moreover, Electrochemical Impedance Spectroscopy (EIS) is also extensively performed to give a quantitative evaluation of the cycling results. In fact, it has been shown that EIS can be used to determine the occurrence of Li-plating.[31] Moreover, of all the non-invasive methods available for the detection of degradation in a lithium-metal cell, EIS is reported to be the fastest, making it a suitable method when characterization needs to be performed frequently.[32] This also makes it congruous with potential implementation on a battery management system (BMS) for periodic measurements. Hence, the performance of the developed separator is evaluated quantitatively.

Results and Discussion

Preparation of the Porous P(VDF–TrFE) Membranes by NIPS

The homogeneity of membranes produced by NIPS is strongly dependent on the composition of the coagulation bath. We found that a 3:1 ethanol-to-water ratio leads to the most defect-free membranes. As shown in Figure 2a), the amount of water in ethanol (EtOH) is gradually increased and it was observed that the appearance changes from a matte white to a non-uniform film with transparent areas. The membrane made in pure EtOH is brittle, breaking when manipulated. When adding 1 part of water for 3 parts of EtOH, the film becomes more robust and flexible. As more water is added, transparent areas gradually appear. The white look is desirable because it indicates the formation of a porous structure, while the transparent sections are caused by a lack of pores.

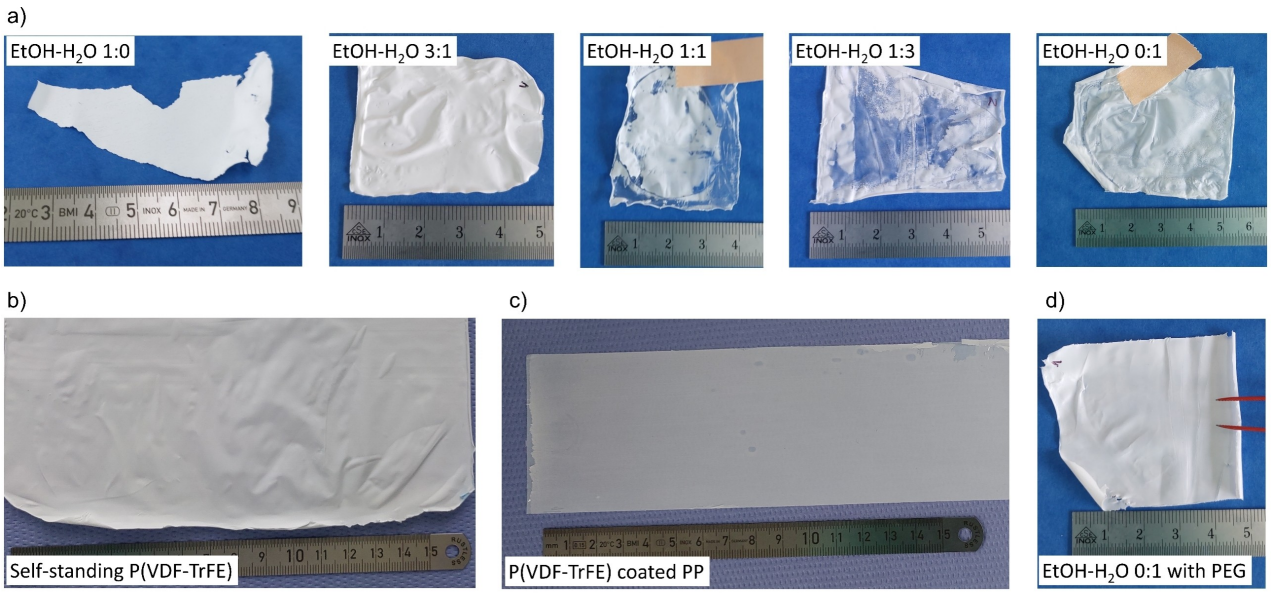

Figure 2. P(VDF–TrFE) membranes produced by NIPS. a) Demonstration of the change in the homogeneity of the membrane with an increasing amount of water in an EtOH coagulation bath. b) Self-standing P(VDF–TrFE) made by casting a slurry on a glass substrate. c) PP separator coated by P(VDF–TrFE) using NIPS. d) Promotion of homogenous pore formation by adding PEG 10 k.

This difference in the morphology is associated with the change in the kinetics of the exchange of the solvent, DMF, with the non-solvent, the EtOH–H_2O mix. Water has a better affinity to DMF than EtOH. By adding water to the coagulation bath, the solvent-non-solvent exchange rate increases, and the membrane formation is faster. The quality of the porous structure is dictated by the formation of polymer-rich and polymer-lean phases in the submerged film as the non-solvent enters it. In pure EtOH, the exchange is slow, which gives time for the two phases to grow and eventually causes coalescence. The latter is detrimental to the mechanical integrity of the membrane because it yields a bicontinuous morphology.[33] Water promotes a fast insertion of the non-solvent. If well balanced, it gives a well-dispersed porous structure, if too fast, it forces an inhomogeneous phase separation. This leads to an asymmetric structure where macro voids gradually appear. The same observations have already been reported.[29] The composition of the coagulation bath must be designed to promote a balanced phase separation. Moreover, to promote the formation of a homogenous film, polyethylene glycol (PEG 10 k) is added to the slurry. The influence of the addition of 5% PEG 10 k on the membrane formation is shown with a coagulation bath of water in Figure 2c). The positive impact on the membrane homogeneity is attributed to the hydrophilic nature of PEG 10 k, which promotes the nucleation of the polymer-lean phases, hence leading to a well-disturbed porous structure.[34] The latter is investigated in the next subchapter by SEM imaging. These findings allow the preparation of defect-free membranes as wide as 20 cm, Figure 2b). To yield the P(VDF–TrFE) coated PP separator, we began by using the same process as for the PVDF membranes, with the difference that instead of casting on a glass substrate, we were casting directly on the PP separator. However, it was quickly realized that the P(VDF–TrFE) coating was clogging the pores of the PP separator, because, as it can been seen Figure S1, coin cells assembled with said separator were not cycling. We have therefore developed what is, therefore, developed a novel process, to the best of our knowledge, a method of preventing pore-clogging, which consists in pre-soaking the PP separator with DMF, and then casting the P(VDF–TrFE) slurry on it, yielding a homogenous coating on the PP separator, see Figure 2c. Due to the pre-soaking process, DMF occupies the pores of the PP separator, thereby hindering the infiltration of the P(VDF–TrFE) slurry during coating and ultimately preventing the solidification of P(VDF–TrFE) within the pores.

Characterization of the P(VDF–TrFE) Membranes

To validate the electroactive nature of the membranes produced by NIPS, structural analyses are performed. Then, an investigation of the porous structure is carried out to validate the use of the membranes as battery separators. First, by means of differential scanning calorimetry (DSC), the first ramp-up curves of the P(VDF–TrFE) powder and the self-standing membrane are compared, as shown in Figure 3a). It is found that the two samples behave identically, showing a curing temperature at ca. 95 °C and a melting point at 150 °C. The overlay of the DSC curves confirms that the processing step did not affect the polymer structural organization. The presence of the Curie temperature at 98 °C proves that the ferroelectric β-phase has crystalized. In a secondary structural analysis, Fourier Transform Infrared Spectroscopy (FT-IR) spectra obtained from the same samples show the almost exclusive presence of the β-PVDF phase as illustrated in Figure 3b). The distinctive signals corresponding to the β-PVDF phases are well-established, making their identification and verification feasible through this method. Additionally, 1H-NMR is carried, see Figure S2. The composition of the copolymer can be determined using these signals and has been evaluated here to 29 mol% of TrFE and 71 mol% of VDF which is in accordance with the composition specified in the certificate of analysis. No significant difference

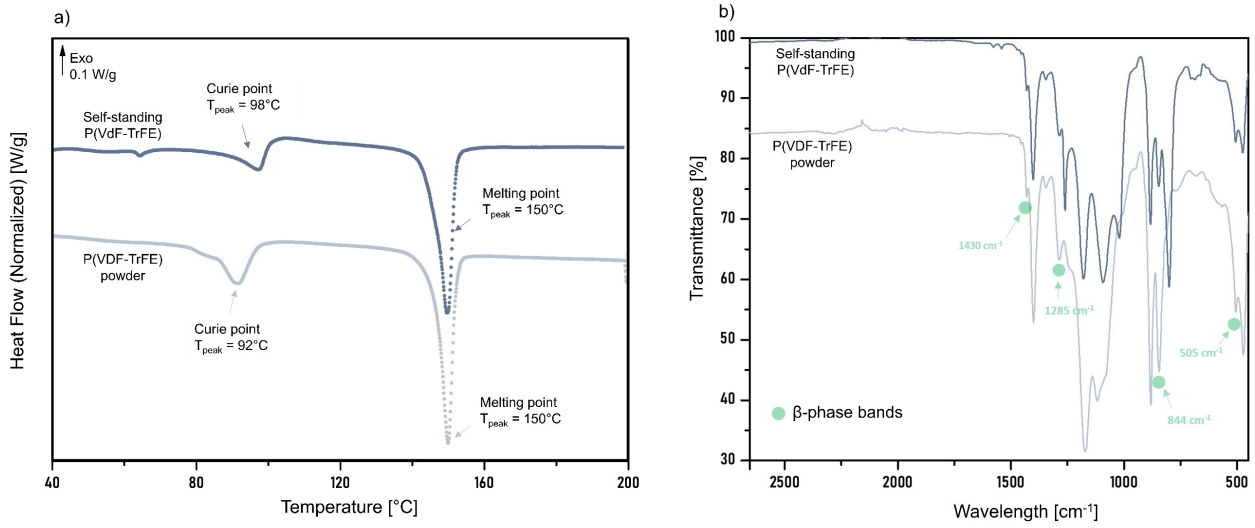

Figure 3. a) DSC curves of the first heating ramp of the P(VDF–TrFE) and the self-standing P(VDF–TrFE) membrane b) FTIR spectra of the P(VDF–TrFE) powder and the self-standing P(VDF–TrFE) membrane.

Research Article
doi.org/10.1002/batt.202300591
Chemistry Europe
European Chemical Societies Publishing

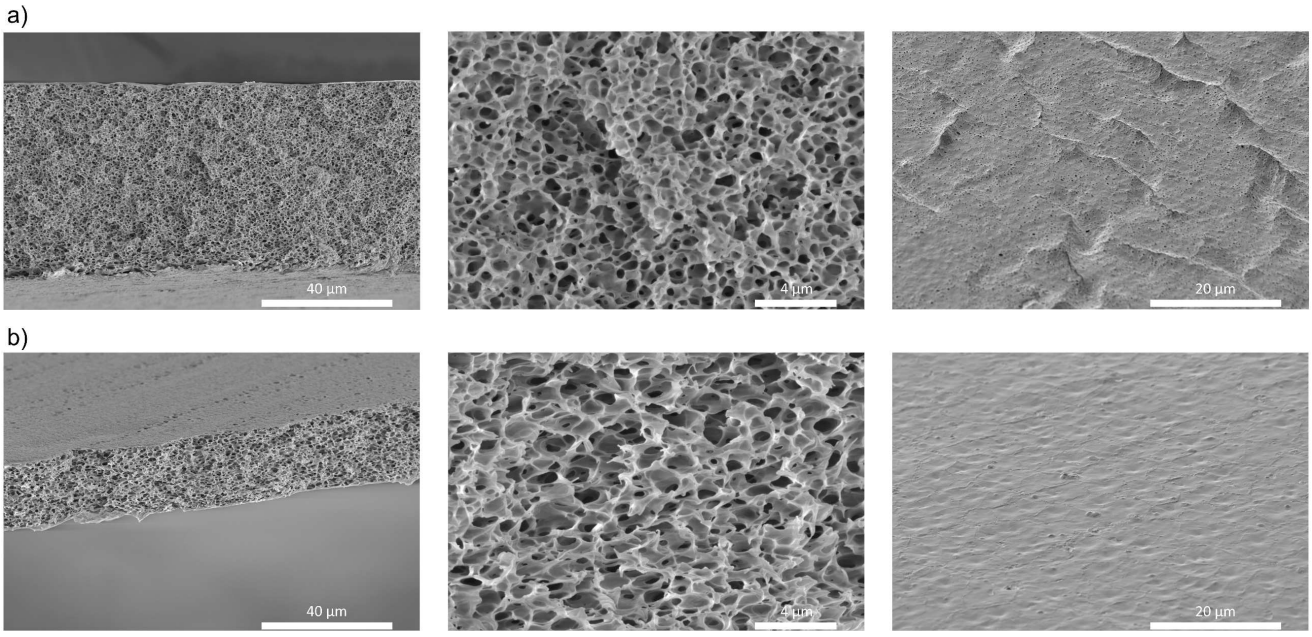

Figure 4. Morphology of the porous membranes made by NIPS. a) Self-standing P(VDF–TrFE) b) P(VDF–TrFE) layer manually delaminated from the P(VDF–TrFE) coated PP separator.

in characteristic peaks is observed in the self-standing P-(VDF–TrFE) membrane, validating that the NIPS method is suitable to yield ferroelectric membranes.

Furthermore, we assessed the piezoelectric constant, d33, for discs composed of both self-standing P(VDF–TrFE) and P(VDF–TrFE)-coated separators. Measurements were conducted both before and after polarization with a coercive field of 10 kV, as outlined in the supplementary Table S1. Notably, a substantial increase in the piezoelectric constant was observed post-polarization. However, due to recurrent dielectric breakdowns during the polarization process, we concluded that membrane poling is unsuitable for the production of separators intended for pouch cells. Therefore, for the single-layer Li-metal pouch cells the membranes are used as-prepared by NIPS.

The porous structure of both the self-standing P(VDF–TrFE) membrane and the P(VDF–TrFE)-coated separator is examined through SEM imaging, with cross-sections and top views displayed in Figure 4. Qualitatively, the structures of the self-standing P(VDF–TrFE) and the coating are similar, exhibiting a homogeneous distribution of pores without macro voids. The morphology of pore structure is cellular, consisting of interconnected spherical pores and thin polymeric walls, aligning with commonly reported configurations. Digital analysis of the images provides estimates for porosity and average pore size, detailed in Table 1. The porosity is approximately 50 %. For both samples, the average pore size is estimated to be ca. 500 nm with a large spread, with maximum values staying below 1 µm. This indicates that the membranes are fit to serve as a separator for battery applications. The top view displays an almost closed surface, with the appearance of small pores. Such morphology is desired, as one wants to maximize the direct contact of P(VDF–TrFE) to the Li-metal surface. To minimize the appearance of pores on their surface, we noticed that the waiting time before immersion plays an important role. When it is decreased, larger pores appear on the surface, as shown in Figure S4.

In addition, the permeability of the prepared samples is assessed by measuring the Gurely number, which is the time required to force a fixed volume of air through the membranes. The value increases as the membrane becomes less permeable to air. This is the case when the porosity decreases, the thickness increases and/or the tortuosity of the pore structure increases. We observed that although the self-standing P-(VDF–TrFE) is twice as thick as the PP separator, the Gurley is only 1.25 times greater. This is an indication that the pore

Table 1. Properties of the P(VDF–TrFE) membranes.

	Thickness [µm]	Porosity [%]	Pore size [nm]	Gurley number [s/100 ml/inch^2]	Ionic conductivity [mS/cm]
PP separator	27	40	<1000	274	$0.98+/-0.09$
Self-standing P(VDF–TrFE)	62	55	499 ± 323	341	$0.91+/-0.13$
P(VDF–TrFE) coated PP	48	47	505 ± 380	24'440	$0.65+/-0.02$

Research Article
doi.org/10.1002/batt.202300591
Chemistry Europe
European Chemical Societies Publishing

structure is well interconnected and has low tortuosity. This is not the case for the P(VDF–TrFE)-coated separator, whose Gurley number is two orders of magnitude greater than the bare PP separator. We hypothesize that despite the use of the pre-soak step, a significant number of pores are clogged by the coating. Surprisingly, the ionic conductivity of the three separators is similar, close to 1 mS/cm. Supposedly, this is possible due to the excellent affinity of the polymer with the liquid electrolyte. To validate the membranes as potential separators for Li-metal batteries, CR2032 coin cells are assembled and tested. It is quickly noticed that the cells assembled with the self-standing P(VDF–TrFE) are prone to short-circuits and fast capacity fading. If instead, the self-standing P(VDF–TrFE) is coupled with a PP separator, the coin cells show reproducible cycling without the appearance of shorts. This double layer configuration is what motivated us to directly coat the P(VDF–TrFE) on the PP separator. Coin cells CR2032 with both the double layer configuration and the coated PP showed improved cycling performance to cells without a P(VDF–TrFE) layer, see Figure S3.

Pouch cell characterization

Three types of single-layer pouch cells are assembled. For the reference cells (referred as REF hereafter), the cathode is NMC 532 with an areal loading of 3 mAhcm^{-2}. Two layers of PP are used as a separator. The anode is a 50 μm thick Li-metal extruded on copper. The chosen electrolyte is a carbonate-based electrolyte with a high fluoroethylene carbonate (FEC) content and lithium tetrafluoroborate salt (LiBF4) from E-Lyte Innovations GmbH. In the second type of cell, the layer of PP that is facing the anode is replaced by the self-standing P(VDF–TrFE) membrane (PVDF–l hereafter). The third type of cell replaces the two separator layers with the P(VDF–TrFE) coated PP (PVDF-c hereafter).

The cycling performance of the pouch cells with the modified separators is compared in Figure 5a). For each condition, five cells are tested. The markers are the average of the discharge capacity measured every five cycles, while the shaded area is the standard deviation. The actual data points from all cells are showed in Figure S5. The PVDF-l cells degrade the fastest, retaining 80% of the initial capacity for about 20 cycles. The PVDF-c and REF cells have similar average capacity in the beginning; however, the REF cells show a steeper capacity fading as compared to the PVDF-c cells Together with the reduced standard deviations, this shows that the PVDF-c cells are the most durable and consistent of the categories, followed by REF cells and finally the PVDF-l cells. The same trend appears in Figure 5b), where the coulombic efficiency (CE) of the cells is displayed. During the first 40 cycles, the CE of the REF and the PVDF-c cells overlap. From this point, the CE of the REF starts decreasing, while the CE of the PVDF-l cells only start doing it after 70 cycles. The cause of death is investigated post-mortem, see Figure S6. It is observed that the both the REF and the PVDF-l present some Li-metal below the dead Li layer. This shows that the cause of failure of the pouch cells is most likely electrolyte depletion, as the continuous formation of dead Li consumes electrolyte. For the PVDF-l cells, no Li-metal is visible on the anode, indicating that failure is due to full consumption of the Li inventory. SEM images of the dead Li layer, Figure S7, reveal that the dead Li of PVDF-l is made of larger bodies compared to the dead Li of PVDF-c, which explains the faster exhaustion of Li reservoir.

Finally, we correlated the cell performance with the EIS investigations. The impedance of each cell is monitored at each cycle. By looking at the Nyquist plots, as displayed in Figure 6a), one can notice that the initial impedance, after forming, of REF cells and PVDF-c is comparable, while the one of PVDF–l is twice as large. This indicates that the forming cycles generated a significant amount of dead Li for the latter category. This is a preliminary suggestion that the P(VDF–TrFE) mitigates the

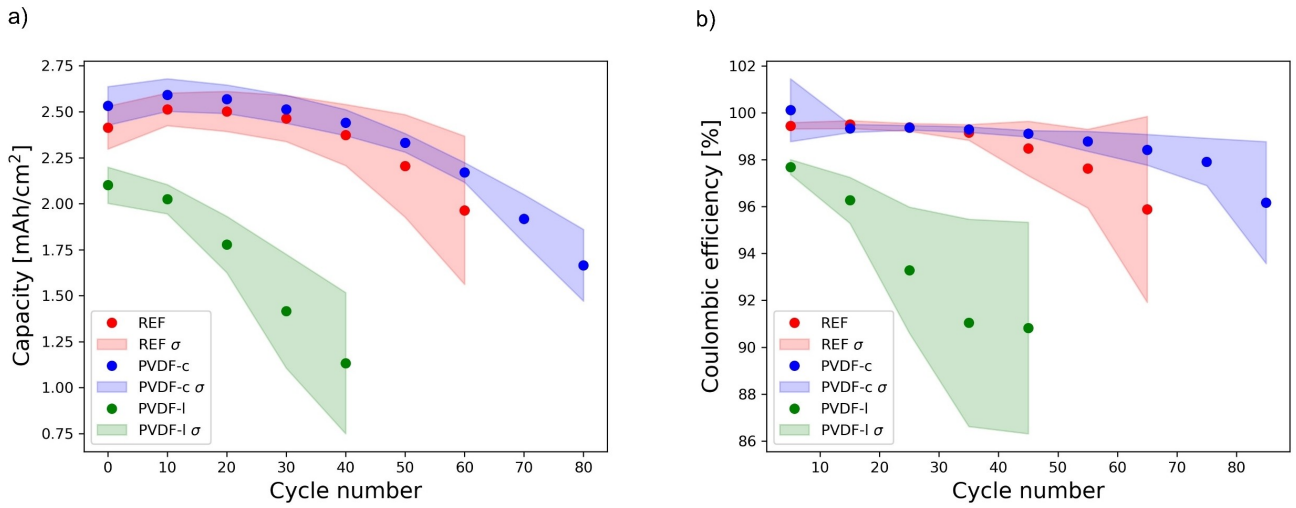

Figure 5. Cycling performance of the single-layer Li-metal pouch cells with modified separators: two layers of PP (REF), the P(VDF–TrFE) coated PP (PVDF-c) or the self-standing P(VDF–TrFE) with a layer of PP (PVDF-l). The colored areas represent the variance [σ] a) discharge capacity an b) coulombic efficiency of the tested pouch cells

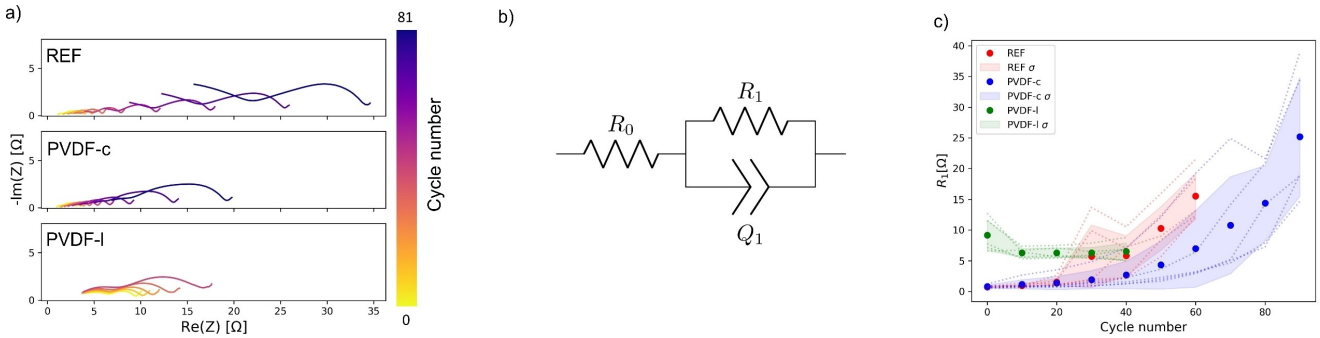

Figure 6. EIS investigation of the single-layer Li-metal pouch cells without or with P(VDF–TrFE) membranes in the separator layer a) Nyquist plots for one representative cell for each pouch category. b) Equivalent Circuit Model (ECM) used to fit the EIS data c) Evolution of R_1 as a function of the cycle number. The solid dots show the mean R_1 value for 5 cells while the shaded areas show the standard deviation, the R_1 is representative of the resistance of the dead Li layer. I. Mochida, Y. Korai, C.-H. Ku, F. Watanabe, Y. Sakai,

increases in the internal resistance of the battery. The raw data of the EIS data is presented in Figure S8.

For the REF and PVDF-c cells, it is observed that as the cell is cycled, a second semi-arc appears at the high-frequency of the EIS, indicating the rise of a new interface. We attribute this arc to the resistance increase due to the generation of a layer composed of dead Lithium. In fact, the formation of dead lithium covers the anode with a layer of lithium that is electrically insulated from the anode by the SEI layer, which in turn increases the ionic path of Li+ because of the increased tortuosity and reduced volume available for Li+ transport. The generation of this layer also creates a new interface inside the cell, which adds to cell's polarization due to the formation of a Li^+ concentration gradient. The analysis of this semiarch can provide an index for the effectiveness of the developed separator. For this purpose, we fit the EIS data to an Equivalent Circuit Model (ECM) in Figure 6b), an example of the fitting curve is shown in Figure S8. The first semiarch from the EIS spectra is fitted to an ECM with a resistor (R_0) connected in series to a resistor (R_1) and constant phase element (Q_1) parallel branch. The value of R_1 indicates the width of the first semiarch, which we attribute to the growing dead Li layer. Hence, determining this value can be used to measure the effectiveness of the separator developed. Figure 6c) shows the evolution of the average value of R_1 for the 5 cells of each category over the cycles, along with the standard deviation. It is seen that the value of R_1 increases rapidly after it crosses 5 Ω. Considering this value as the threshold for dead lithium covering the entire surface of the anode, the REF cells reach this value at around 30 cycles while the PVDF-c cells reach this value at about 50 cycles, resulting in a delay of 20 cycles. It can be noticed that at failure both configurations show an average R_1 of ca.15 Ω, suggesting that the dead Li at this point should be comparable independently of the separator layer. This is indeed what is observed in the post-mortem inspection, in Figure S7, where the morphology and the thickness of the dead Li layer of the REF and the PVDF-I cells is qualitatively comparable, reinforcing the assignment of R1 to the resistance of the dead Li layer. These findings imply that the ferroelectric coating plays a pivotal role in retarding the thickening of the dead lithium layer. Moreover, such a diagnostic technique could potentially be implemented in an EIS-capable BMS which would help to continuously monitor the safety of the cells.

Further investigation is essential to pinpoint the precise cause of the advantageous effect of the ferroelectric coating. Plausible explanations include the prospect that deformation induced by dendrite growth triggers ferroelectric domain activation, thereby regulating Li^+ flux. Another consideration is the reduction of PVDF by Li-metal, possibly resulting in a LiF-enriched solid electrolyte interphase. Nevertheless, our compelling evidence establishes that a ferroelectric coating alone is insufficient to impede the growth of lithium dendrites; effective mitigation requires coupling with a conventional separator.

Conclusions

In conclusion, we demonstrated, for the first time, the utilization of P(VDF–TrFE) as a ferroelectric copolymer in the fabrication of membranes through NIPS as a potential solution to address the critical challenge of dead lithium formation in Li-metal anodes coupled with carbonate electrolytes. This study showcases the synthesis of both self-standing membranes and coatings on polypropylene (PP) separators, revealing a homogenous cellular pore structure and without hindering the ionic conductivity of the separator. The comprehensive evaluation in relevant pouch cell formats, featuring a thin Li metal anode (50 μm), a high-loading NMC532 cathode (3 $mAhcm^{-2}$), and a carbonate electrolyte, highlights the superior performance of cells employing P(VDF–TrFE)-coated PP separators. The observed slower and more consistent capacity fading, coupled with the slowest increase in impedance determined through Electrochemical Impedance Spectroscopy investigations, highlights the beneficial role of the ferroelectric material in effectively mitigating the growth of the dead lithium layer. This work contributes valuable insights to the ongoing efforts in advancing lithium-metal battery technologies and underscores the potential of P(VDF–TrFE) as a key enabler for enhanced electrochemical performance and longevity in practical applications.

Experimental Section

Preparation of the Porous P(VDF–TrFE) Membranes by NIPS

The P(VDF–TrFE) (Piezotech), PEG 10 k (Sigma), DMF (Sigma) weight ratio is set to 18:5:77. The solid components are added to the solvent and mixed with a planetary centrifugal mixer, ARE-250, Thinky, 3 times for 4 min at 2000 rpm with 5 min rest steps in between. It is important to prevent overheating of the slurry to avoid color changes. The slurry is cooled to 25 °C before casting. The relative humidity in the room is not controlled. To produce the self-standing membrane, films with a wet thickness of 250 μm are cast with a blade coater on a glass substrate. For the PVDF-coated PP, the latter is soaked with DMF before casting the film on it. The soaking step is essential to prevent excessive pore clogging. With a close wound meter bar coater, a 40 μm thick film was coated on top of the PP separator. In either case, the films rest for 30 sec in the air before immersion into the coagulation bath, in which they sit for 5 min. The rest step is fundamental to yield a compact surface of the polymer. Then they are moved to a bath of deionized water for 2 min to remove the remaining solvent. Follows drying in a convection oven at 60 °C for 30 min.

Characterization of the P(VDF–TrFE) Membranes

The Gurley value as an estimation of the air permeability of the porous membrane is measured with Gas Permeameter GP-101A-G-T200 from Porous Materials Inc. The ionic conductivity is measured with an Octostat 30, Ivium, with a potential amplitude of 20 mV applied vs. OCP from 1 Mhz to 0.1 Hz. Stainless steel spacers (316 s, 16 mm diameter) are used as blocking electrodes in CR2023 coin cells. The conductivity is taken at the intercept with the real axis in the Nyquist plot. Differential Scanning Calorimetry (DSC) measurements are carried out using DSC Q2000 instrument (TA INSTRUMENTS). The data is recorded with Advantage software and analyzed with TRIOS software. The calorimeter is calibrated using an indium standard (heat flow and temperature calibration). The sample (around 5–7 mg) is placed into 40 μL Tzero hermetic pan with manual pierced lid. Nitrogen at 50 mL min^{-1} is used as a purge gas. Main thermal behaviors are investigated at a heating rate of 10 °C . min^{-1} using temperature ramps of (1) heating from 30 to 200 °C; (2) cooling from 200 to 30 °C; (3) heating from 30 to 200 °C. 1H NMR spectrum of P(VDF–TrFE) materials are obtained using Bruker Advance 300 (300 MHz) spectrometer equipped with a QNP probe at room temperature. Acetone-d6 is used as deuterated solvent. Chemical shifts (δ) are given in ppm referenced to the residual deuterated solvent peak. Fourier Transform Infrared Spectroscopy (FT–IR) of the sample is operated on a spectrum two infrared spectrophotometer (PerkinElmer) with a LiTaO3 (lithium tantalate) detector using a Diamond UATR accessory unit. The samples are then placed directly on the ATR crystal. The spectra are acquired with 16 scans from 4000 to 450 cm^{-1} in transmission mode in air through a resolution of 4 cm^{-1}. The Spectrum 10 software from PerkinElmer is used to record and process the data.

Pouch Cell Assembly

For testing we build pouch cells with one pair of electrodes and nominal capacity of 67 mAh. First, the positive electrodes, separator and pouch foil are prepared outside the glove box. The positive LiNi0.5 Mn0.3Co0.2O2 (NMC532) electrode is cut with an infrared nanosecond-pulsed fiber laser into sheets. The NMC532 electrode is prepared by project partner Belenos and has a capacity of 3 mAh cm^{-2}. Further, we size the separator and pouch foil into the correct dimensions with a blade. Subsequently the prepared materials are dried in a heated vacuum chamber at 65 °C for approximately 16 hours before being transferred into the argon-filled glovebox. As negative electrode we use commercial lithium metal with 0.3% aluminum content laminated on a copper substrate. The lithium metal electrode is cut into sheets inside the glovebox using a mechanical die. We then stack the electrode and separator sheets, fix a tab to the current collector foil using ultrasonic welding and insert the stack into the pouch foil. Using an electronic pipette, we inject 0.5 mL of electrolyte into the cell. As electrolyte we use a carbonate-based electrolyte with a high fluoroethylene carbonate (FEC) content and lithium tetrafluoroboarate salt (LiBF4) from E-Lyte Innovations GmbH. In the last step the cell is evacuated to 64 mbar and sealed.

Testing Protocol

The testing of the prepared pouch cells is executed by first performing a formation process, followed by a BoL (Beginning of Life) characterization phase and finally a cycling phase. A full description of the forming protocol and a scheme explaining the testing protocol can be found in Figure S9. The characterization phase involves EIS at different OCV (4.2 V, 3.9 V, 3.7 V, 3.5 V, 3 V). It is mainly used to characterize the cells at BoL. It also involves a battery capacity detection (BCD) wherein the cell is CC charged at C/10 up to 4.2 V, and then CV charged at 4.2 V until the current drops to below C/100. This is followed by CC discharge at C/10 until the cell reaches 3 V. The capacity of the cell is taken during this discharge. The cycling phase involves performing four cycles at C/10 followed by a capacity check every 5th cycle. For analysis reasons, diagnostic techniques are intercalated during each discharging phases. Specifically: EIS at OCV~3.9 V and current step-profile consisting of a CC discharge and CC charge at C/10 for a duration of 5 minutes. Every 5th cycle, a capacity check has been performed which is made by a CC charge at C/10 until 4.2 V, CV charge at 4.2 V until a cutoff current of C/100 and a CC discharge at C/10 until 3 V. The cells are stopped at 50% SOH, after which they are deep discharged and moved to a glovebox for post-mortem inspection.

Supporting Information

The authors have cited additional references within the Supporting Information.[30,31]

Acknowledgements

This work was carried in the frame of the European project 'HIDDEN'. The project has received funding from the European Union's Horizon 2020 research and innovation programme under grant agreement No. 957202.

Conflict of Interests

The authors declare no conflict of interest.

Data Availability Statement

The data that support the findings of this study are available from the corresponding author upon reasonable request.

Keywords: EIS · ferroelectric · dead-Li · Li-metal · PVDF

[1] J. T. Frith, M. J. Lacey, U. Ulissi, *Nat. Commun.* **2023**, *14*, 420.
[2] M. Li, J. Lu, Z. Chen, K. Amine, *Adv. Mater.* **2018**, *30*, 1800561.
[3] B. Acebedo, M. C. Morant-Miñana, E. Gonzalo, I. Ruiz de Larramendi, A. Villaverde, J. Rikarte, et al., *Adv. Energy Mater.* **2023**, *13*, 2203744.
[4] D. Lin, Y. Liu, Y. Cui, *Nat. Nanotechnol.* **2017**, *12*, 194.
[5] E. Winter, T. J. Schmidt, S. Trabesinger, *Batteries & Supercaps* **2022**, *5*, e202100145.
[6] J. Xiao, Q. Li, Y. Bi, M. Cai, B. Dunn, T. Glossmann, et al., *Nat. Energy* **2020**, *5*, 561.
[7] J. Xu, R. D. Deshpande, J. Pan, Y.-T. Cheng, V. S. Battaglia, *J. Electrochem. Soc.* **2015**, *162*, A2026.
[8] M. Srout, M. Carboni, J.-A. Gonzalez, S. Trabesinger, *Small* **2023**, *19*, 2206252.
[9] A. Jana, S. I. Woo, K. S. N. Vikrant, R. E. García, *Energy Environ. Sci.* **2019**, *12*, 3595.
[10] C. Fang, J. Li, M. Zhang, Y. Zhang, F. Yang, J. Z. Lee, et al., *Nature* **2019**, *572*, 511.
[11] K.-H. Chen, K. N. Wood, E. Kazyak, W. S. LePage, A. L. Davis, A. J. Sanchez, et al., *J. Mater. Chem. A* **2017**, *5*, 11671.
[12] W. Xu, J. Wang, F. Ding, X. Chen, E. Nasybulin, Y. Zhang, et al., *Energy Environ. Sci.* **2014**, *7*, 513.
[13] J. Janek, W. G. Zeier, *Nat. Energy* **2016**, *1*, 1.
[14] M. Arrese-Igor, M. Martinez-Ibañez, E. Pavlenko, M. Forsyth, H. Zhu, M. Armand, et al., *ACS Energy Lett.* **2022**, *7*, 1473.
[15] Y. Yu, Y. Liu, J. Xie, *ACS Appl. Mater. Interfaces* **2021**, *13*, 18.
[16] C. Fu, V. Venturi, J. Kim, Z. Ahmad, A. W. Ells, V. Viswanathan, et al., *Nat. Mater.* **2020**, *19*, 758.
[17] C. Cui, F. Xue, W.-J. Hu, L.-J. Li, *NPJ 2D Mater. Appl.* **2018**, *2*, 1.
[18] Y. Ji, B. Yuan, J. Zhang, Z. Liu, S. Zhong, J. Liu, et al., *ENERGY Environ. Mater.* **2022**, e12510.
[19] H. Peng, Z. Xu, Y. Zhou, J. Huang, T. Yang, J. Zhang, et al., *J. Materiomics* **2023**.
[20] J. Xiang, Z. Cheng, Y. Zhao, B. Zhang, L. Yuan, Y. Shen, et al., *Adv. Sci.* **2019**, *6*, 1901120.
[21] J. Luo, C.-C. Fang, N.-L. Wu, *Adv. Energy Mater.* **2018**, *8*, 1701482.
[22] J. Ryu, D.-Y. Han, D. Hong, S. Park, *Energy Storage Mater.* **2022**, *45*, 941.
[23] G. Liu, D. Wang, J. Zhang, A. Kim, W. Lu, *ACS Mater. Lett.* **2019**, *1*, 498.
[24] M. Kundu, C. M. Costa, J. Dias, A. Maceiras, J. L. Vilas, S. Lanceros-Méndez, *J. Phys. Chem. C* **2017**, *121*, 26216.
[25] P. Arora, Z. (John) Zhang, *Chem. Rev.* **2004**, *104*, 4419.
[26] V. Deimede, C. Elmasides, *Energy Technol.* **2015**, *3*, 453.
[27] G. R. Guillen, Y. Pan, M. Li, E. M. V. Hoek, *Ind. Eng. Chem. Res.* **2011**, *50*, 3798.
[28] A. K. Hołda, I. F. J. Vankelecom, *J. Appl. Polym. Sci.* **2015**, *132*, app.42130.
[29] T.-H. Young, L.-P. Cheng, D.-J. Lin, L. Fane, W.-Y. Chuang, *Polymer* **1999**, *40*, 5315.
[30] P. Martins, A. C. Lopes, S. Lanceros-Mendez, *Prog. Polym. Sci.* **2014**, *39*, 683.
[31] P. P. Paul, E. J. McShane, A. M. Colclasure, N. Balsara, D. E. Brown, C. Cao, et al., *Adv. Energy Mater.* **2021**, *11*, 2100372.
[32] P. Iurilli, L. Luppi, C. Brivio, *Energies* **2022**, *15*, 6904.
[33] D. R. Tree, L. F. D. Santos, C. B. Wilson, T. R. Scott, J. U. Garcia, G. H. Fredrickson, *Soft Matter* **2019**, *15*, 4614.
[34] L. Zheng, J. Wang, Y. Wei, Y. Zhang, K. Li, Z. Wu, *RSC Adv.* **2016**, *6*, 20926.

Manuscript received: December 13, 2023
Revised manuscript received: January 19, 2024
Accepted manuscript online: January 30, 2024
Version of record online: February 19, 2024